

A mini review of NMR and MRI

Fatemeh Khashami

fatemeh.khashami@utsouthwestern.edu

Department of Internal Medicine, The University of Texas Southwestern Medical Center, Dallas, TX 75390

Department of Physics, The University of Texas at Dallas, Dallas, TX 75080

(Dated: January 4, 2024)

Abstract

Nuclear magnetic resonance (NMR) and magnetic resonance imaging (MRI) are versatile tools with broad applications from physics and chemistry to geology and medical studies. In this mini-review, we consider the concepts of NMR and MRI technologies from their fundamental origins to applications in medical science. We start from a quantum mechanical basis and consider the significant importance of NMR and MRI in clinical research. Furthermore, we briefly introduce different types of NMR systems. We also investigate some of the most important applications of MRI techniques to provide valuable methods for visualizing the inside of the body and soft tissues.

1. INTRODUCTION

Nuclear magnetic resonance (NMR) and magnetic resonance imaging (MRI) are two powerful technologies that help to understand biochemical information at molecular levels and investigate the inside of the human body. NMR is a non-destructive analytical technique that utilizes non-ionizing radio frequency (RF) waves for the chemical description of living and non-living objects. Particularly, MRI is widely operated in medical science for diagnostic imaging [1–4].

NMR and MRI technologies are byproducts of our understanding of the atomic world and the discovery of quantum theory. In fact, it is impossible to comprehensively study the working principles of NMR and MRI without considering quantum physics. In particular, to explain the concepts behind these technologies, we need to understand spin in quantum physics [5–7].

The history of the discovery of quantum spin is one of the most exciting parts in the history of the modern science. This goes back to our understanding of matter in a more profound way, illuminated by the discovery of the elements of atoms. This pioneered by Rutherford’s discovery of the atomic nucleus in 1911 and the Bohr model of the atom in 1913 [8, 9]. Later, de Broglie’s vision of the wave-particle duality challenged the classical physics viewpoint and revolutionized the perspective of quantum mechanics to a greater extent. This radical departure from the classical worldview makes the behavior of quantum systems counterintuitive, which still remains a subject of a heated debate [10–12]. The new perspective of quantum mechanics introduced a new vision of the physical world with manifesting probabilistic outcomes, superposition, and particle entanglement [13, 14].

The foundation for quantum mechanics laid by Heisenberg’s mechanics in 1925 and Schrödinger’s wave equation in 1926. In the same year, Uhlenbeck and Goudsmit discovered electron spin and its intrinsic angular momentum properties. Regarding electron spin and its properties in a quantum system, Paul Dirac revised the hydrogen atom’s spectrum in 1928. Israel Isaac Rabi initiated the principle of NMR technology in 1938, known as Rabi’s discovery. Furthermore, in 1946, Felix Bloch and Edward Purcell developed the first NMR machines. The foundation for NMR is related to the understanding of the Zeeman effect, illustrating how the interaction of nuclear spins with external magnetic fields played a crucial role in developing quantum mechanics [15–17].

The Bloch equation explains the dynamics of the NMR system and describes the spin relaxation dynamics in a quantum spin system. Later, the concept of the NMR signal is described by the Fourier transform (FT) method, corresponding to the free induction decay (FID) signal, to convert

the time domain NMR signal to the frequency domain signal. Additionally, in 1991, Richard R. Ernst followed the FT-NMR method and developed the FT-NMR spectroscopy [3, 18, 19].

It is important to highlight that NMR was the first generation of Rabi's discovery, whereas MRI represents the second generation of this phenomenon. These developed technologies provide practical tools for understanding and describing various medical issues, opening the new way to medical imaging as a diagnostic device for investigating cancerous and normal tissues [20–22].

In this review, we focus on the quantum mechanical foundations of NMR and MRI and attempt to design an understandable foundation for the quantum mechanical framework of these technologies. In other words, this review aims to bridge the gap between the technological application of quantum mechanics and the fundamental principles based on which these technologies are built. Learning the basic frameworks behind the technologies is beneficial for many reasons [4, 23].

2. THE ZEEMAN EFFECT OF NUCLEAR SPINS

To start the physics behind NMR and MRI technologies, we can consider a spin system's behavior in the absence and presence of a magnetic field, \vec{B}_0 . Spins with magnetic dipole moments μ_s are oriented in random directions that are out of phase in general in the absence of a magnetic field. Moreover, their net magnetic moment is zero [21, 23, 24], as we presented in Fig. 1(a). After applying an external magnetic field, \vec{B}_0 , the nuclei precess in phase, which can be along with or against the magnetic field relying on the spin of the nuclei, which is shown in Fig. 1(b) [10, 25].

The magnetic field builds a torque on μ_s of the nuclei and orients it along the z -axis. The nuclear magnetic moment of the nucleus spin aligns with or against \vec{B}_0 , which has $(2I + 1)$ a number of states, which results in Zeeman splitting. This splitting creates $(2I + 1)$ energy levels that are expressed by the spin quantum number, m_s , which has the magnitude $1/2$ and direction $+$ or $-$ along the z -axis [4, 26–29].

From the Zeeman effect, the NMR signal depends on the energy difference between the two-level states of the nucleus. The lower energy level is known as the α state, with $m_s = +1/2$, for which the nucleus is aligned with the magnetic field, and the higher energy level is known as the β state, with $m_s = -1/2$, for which the proton is aligned against \vec{B}_0 . The lower energy level often has slightly more occupants than the higher energy level, in general, [15, 19, 27, 30].

The spin angular momentum in z -axis is $S_z = m_s \hbar = \pm \hbar/2$, and the total magnitude spin angular momentum vector for spin quantum number $1/2$ is $|\vec{S}| = \sqrt{s(s+1)}\hbar = \sqrt{3/4}\hbar$, where \hbar

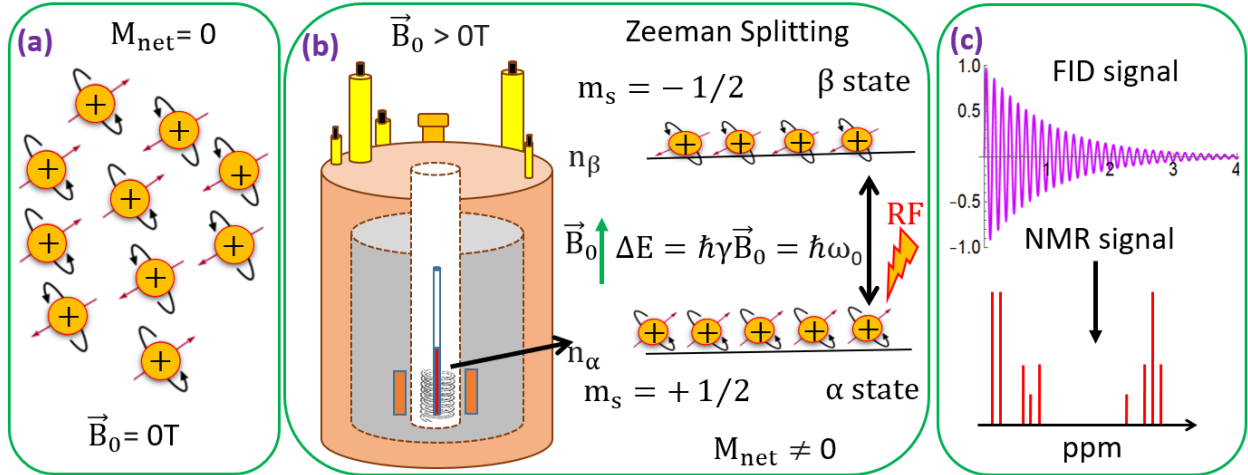


FIG. 1. (a) In the absence of the magnetic field \vec{B}_0 , ^1H atoms lay in random orientations, and their nuclei occupy a single energy level. (b) Due to Zeeman splitting, when the strong magnetic field is applied, some nuclei align parallel to \vec{B}_0 (α state) and others anti-parallel \vec{B}_0 (β state). More of the nuclei occupy the lower energy level. After applying an RF pulse, some nuclei in the lower state move to the higher. (c) When the RF pulse is switched off, the nuclei return to equilibrium and emit a free induction decay (FID) signal. By the Fourier transformation (FT) method, the FID signal converts to the NMR spectrum

is Planck constant, which is equal to 1.054×10^{-34} J.S. The magnetic dipole moment of nuclei, μ_z , with $m_s = \pm 1/2$, is defined as $\mu_z = m_s \hbar \gamma = \pm 1/2 \hbar \gamma$, where γ is gyromagnetic ratio with units MHz/Tesla, and it is a constant value for each nucleus and is related to the magnetic moment μ_s , and the spin number I for a specific nucleus is expressed as

$$\gamma = \frac{2\pi\mu_z}{\hbar I}, \quad (1)$$

where γ can be positive or negative [4, 31–33].

Due to the Zeeman splitting, the interaction energy of a spin state with a magnetic field along the z -axis is directly proportional to the magnetic field strength and is expressed as

$$E = -\vec{\mu} \cdot \vec{B}_0. \quad (2)$$

The energy along the z -axis is given by $E = -\vec{\mu}_z \cdot \vec{B}_0$. Therefore, the energy difference between the two upper and lower energy levels is obtained as

$$\Delta E = E_\beta - E_\alpha = \hbar\gamma\vec{B}_0 = \hbar\omega_0. \quad (3)$$

In this relation, the nucleus spin precess at a specific frequency ω_0 , known as the Larmor frequency, has the unit rad/s. As we can see from Eq. (3), the Larmor frequency, which is the

precession frequency of the spins around the axis of the magnetic field, is $\omega_0 = \gamma \vec{B}_0$ [4, 34]. Using resonant RF pulses, we can excite nuclei in the lower energy state [35–37]. An NMR spectrum usually uses RF pulses in frequency between 60-900 MHz [21, 24, 31]. When the RF pulse is turned off, the nuclei precess around \vec{B}_0 [37, 38].

The Zeeman splitting leads to a net magnetization of the sample, which means that once the magnetic field is turned off, the nuclei flip down, and the magnetization vector approaches equilibrium. Thus, the rotating magnetization vector generates a current in a receiver coil. This current makes the detection of the NMR signal possible. The oscillating signal presents waves with decreasing magnitude as the nucleus re-aligns with the magnetic field. This wave is called a free induction decay (FID) signal. Then, the Fourier transformation (FT) method converts the FID signal to the frequency domain, which appears as peaks along the x -axis of the NMR spectrum. This is called chemical shift and is given in units ppm [see Fig. 1(c)] [22, 37]. We will explain the chemical shift properties later in this review.

3. THE BOLTZMANN DISTRIBUTION OF NUCLEAR SPINS

The Boltzmann distribution describes the number of nuclei in each spin state. At room temperature, the number of spins in the lower energy level (n_α) is greater than the number in the higher energy level (n_β). However, the energy separation between these two states is relatively small. Therefore, the number of nuclei at each spin state depends upon the temperature of the sample [4, 22, 36, 39].

The Boltzmann distribution shows that the NMR signal intensity is proportional to the applied magnetic field and inverse to the temperature. The weak magnetic moments of nuclear spins cause small differences in the nuclear spin populations [40–42]. In other words, the NMR signal is proportional to the nuclear polarization P , governed by the Boltzmann distribution of nuclear spins on the Zeeman energy levels. In thermal equilibrium, for a spin-1/2 system, it is determined by a thermal population difference determined by the Boltzmann factor as

$$P = \tanh \frac{\gamma \hbar B_0}{2k_B T}, \quad (4)$$

where P is the spin polarization, T is the temperature, and k_B is the Boltzmann constant. The relative number of upper and lower population is given by $n_\alpha + n_\beta = n_0$, where n_0 is the number of nuclei per unit volume [26, 43, 44].

At thermodynamic equilibrium, the ratio between the populations of the two levels can be written as

$$\frac{n_\alpha}{n_\beta} = \exp\left(\frac{-\Delta E}{k_B T}\right) = \exp\left(\frac{-\hbar\omega_0}{k_B T}\right) \approx 1 - \frac{\hbar\omega_0}{k_B T}. \quad (5)$$

From Eq. (5) we have [4]

$$\begin{aligned} n_\beta &= \frac{n_0}{1 + e^{\beta\hbar\omega_0}} \cong \frac{n_0}{2 + \beta\hbar\omega_0} = \frac{n_0}{2} \frac{1}{1 + \beta\hbar\omega_0/2} \cong \frac{n_0}{2} \left(1 - \frac{\beta\hbar\omega_0}{2}\right), \\ n_\alpha &= \frac{n_0}{1 + e^{-\beta\hbar\omega_0}} \cong \frac{n_0}{2 - \beta\hbar\omega_0} = \frac{n_0}{2} \frac{1}{1 - \beta\hbar\omega_0/2} \cong \frac{n_0}{2} \left(1 + \frac{\beta\hbar\omega_0}{2}\right). \end{aligned} \quad (6)$$

Moreover, the magnetization can be calculated for the spin 1/2 system in terms of the T and \vec{B}_0 . The total magnetization is expressed as $M_0 = n_\alpha \mu_z^{(\alpha)} + n_\beta \mu_z^{(\beta)}$, that is the sum of all the spins in the sample known as Bulk magnetization. At equilibrium, the magnetization aligned with \vec{B}_0 is given by Curie's law of spin 1/2 nuclei as

$$M_0 = (n_\alpha - n_\beta) \frac{\gamma\hbar}{2} \cong \frac{\gamma\hbar}{2} n_0 \frac{\hbar\omega_0}{2k_B T} = \frac{n_0 \gamma^2 \hbar^2}{4k_B T} B_0 = \chi_0 B_0, \quad (7)$$

where χ_0 is the static nuclear susceptibility of a sample, which shows how the system becomes magnetized in \vec{B}_0 , and it is inversely proportional to the T .

4. CHEMICAL SHIFT

The chemical shift can determine molecules' structure and functional groups in the NMR spectrum. Since the chemical shifts represent protons, they must absorb different amounts of energy to attain many peaks due to magnetic shielding. All protons are surrounded by electrons that shield them from \vec{B}_0 , and the more circulating electrons, the more shielding effect occurs [see Fig. 2(a)] [1, 19, 45]. The amount of shielding is directly associated with the electron density around 1H nucleus. The higher shielded electrons need higher energy for the resonance.

The effective magnetic field, \vec{B}_{eff} , experienced by a nucleus is the sum of \vec{B}_0 and the induced magnetic field, \vec{B}_{ind} , which is generally less than \vec{B}_0 , and can be expressed as

$$\vec{B}_{\text{eff}} = \vec{B}_0 + \vec{B}_{\text{ind}} = \vec{B}_0(1 - \sigma), \quad (8)$$

where σ is the shielding constant. According to Lenz's Law, \vec{B}_0 that influence the electron density of the proton of 1H atom that opposes \vec{B}_{ind} is given by $\vec{B}_{\text{ind}} = -\sigma\vec{B}_0$. The nucleus in various local environments experiences slightly different frequencies from ω_0 , which is called effective

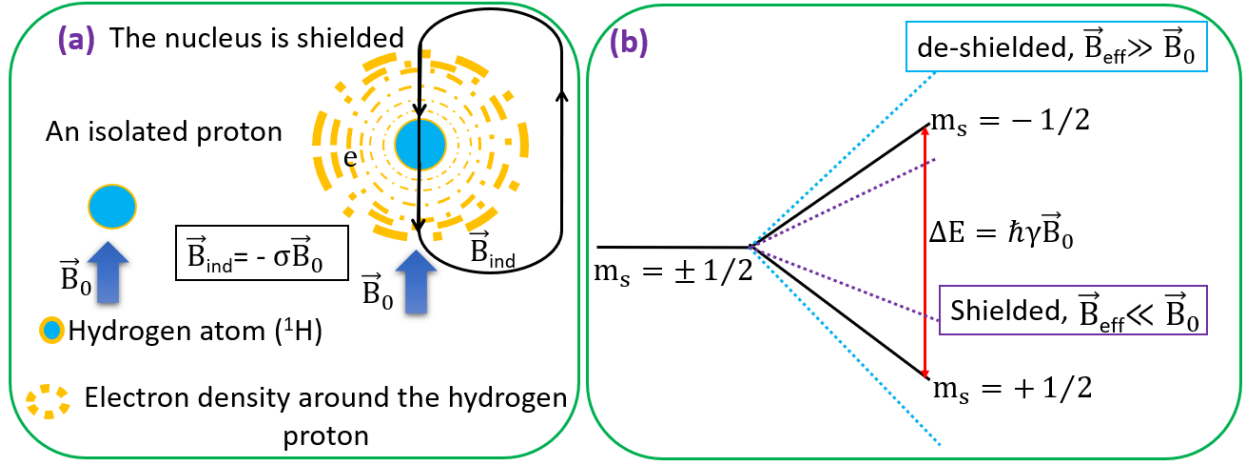


FIG. 2. (a) In Hydrogen nuclei, electrons change the effective magnetic field (\vec{B}_{eff}) experienced by atoms. The external field (\vec{B}_0) induces currents around the nucleus. The induced magnetic field (\vec{B}_{ind}) is opposite in the direction to \vec{B}_0 , and the electrons shield the nucleus. (b) For spin quantum number $1/2$, there is $(2I + 1)$ degeneracy, the energy difference between the two states is $\Delta E = \hbar \gamma \vec{B}_0$. When \vec{B}_{eff} is less than \vec{B}_0 , the nucleus becomes shielded, and when \vec{B}_{eff} is more than \vec{B}_0 , it becomes de-shielded

Larmor frequency ω_{eff} [28, 45, 46]. The shielding constant for a particular nucleus in a particular environment is given by

$$\omega_{eff} = \gamma \vec{B}_{eff} = \gamma \vec{B}_0 (1 - \sigma). \quad (9)$$

From Fig. 2(b), when \vec{B}_{eff} at the position of the nucleus is less than \vec{B}_0 , the nucleus gets shielded. Otherwise, the nucleus is considered de-shielded. In the shielding, the electron density circulates about the direction of \vec{B}_0 and opposes the external magnetic field, reducing \vec{B}_{eff} . As a result of the electron shielding, the nucleus experiences different frequencies, commonly known as the chemical shift, denoted by δ , and expressed in parts-per-million (ppm).

The chemical shift of sample, δ_s with the resonance Larmor frequency of the sample ω_s , is independent of \vec{B}_0 and is dependent on the environment of the nucleus. By considering the resonance Larmor frequency of an internal reference, ω_{ref} , the chemical shift of the sample in ppm can be attained as

$$\delta_s = 10^6 \times \frac{\omega_s - \omega_{ref}}{\omega_{ref}}. \quad (10)$$

5. THE BLOCH EQUATIONS DESCRIPTION

The signal measured in an NMR sample is due to the existence of net magnetization, \vec{M} , which was first proposed in 1946 by Felix Bloch [15, 30, 47]. Central to the NMR technology is the concept of the relaxation of the net magnetization. The relaxation is due to spin-lattice and spin-spin relaxations in the system. Therefore, in this process, the spins decohere and relax to their ground states [48–50]

Spin-lattice relaxation or longitudinal relaxation is the process by which the net magnetization returns to the z -axis, known as the longitudinal magnetization, M_z . In this scenario, the net magnetization is aligned with the external magnetic field [43, 51]. This process is due to energy exchange between the spin system and neighboring molecules. By switching off the RF pulses, $\sim 63\%$ of the magnetization returns to thermal equilibrium [52, 53]. The spin-lattice relaxation rate is governed by a constant value, T_1 , an important quantity in NMR spectroscopy. T_1 determines how quickly the spin of the nucleus becomes parallel to the magnetic field [see Fig. 3(a)-(b)] [45, 54].

On the other hand, spin-spin relaxation or transverse relaxation is a process due to interaction between the spin system and their magnetic field on the $x - y$ plane, known as transverse magnetization, M_{xy} . When an RF pulse is switched off, M_{xy} decays to zero with the time constant T_2 , where only $\sim 37\%$ of original M_{xy} is present [see Fig. 3(c)-(d)] [22, 36, 51, 55].

In the relaxation process, the magnetization returns to equilibrium along the z -axis and in the $x - y$ plane at different rates. According to the Bloch equation, the dynamics of the net magnetization is given by

$$\frac{d\vec{M}}{dt} = \vec{M} \times \gamma \vec{B} - \frac{M_x \hat{i} + M_y \hat{j}}{T_2} - \frac{(M_z - M_0) \hat{k}}{T_1}, \quad (11)$$

where M_x , M_y , and M_z are the components of magnetization \vec{M} in the x , y and z directions, and M_0 is the magnetisation at the steady state. Also, T_1 and T_2 are the spin-lattice and spin-spin relaxation times, respectively. Considering each of the Bloch components in magnetic field (B_x , B_y , B_z), we attain

$$\frac{dM_x(t)}{dt} = \gamma (M_y(t)B_z(t) - M_z(t)B_y(t)) - \frac{M_x(t)}{T_2}, \quad (12)$$

$$\frac{dM_y(t)}{dt} = \gamma (M_z(t)B_x(t) - M_x(t)B_z(t)) - \frac{M_y(t)}{T_2}, \quad (13)$$

$$\frac{dM_z(t)}{dt} = \gamma (M_x(t)B_y(t) - M_y(t)B_x(t)) - \frac{M_z(t) - M_0}{T_1}. \quad (14)$$

For $B_x = 0$, $B_y = 0$, and $B_z = B_0$, the rate of change of magnetization from the Bloch equation

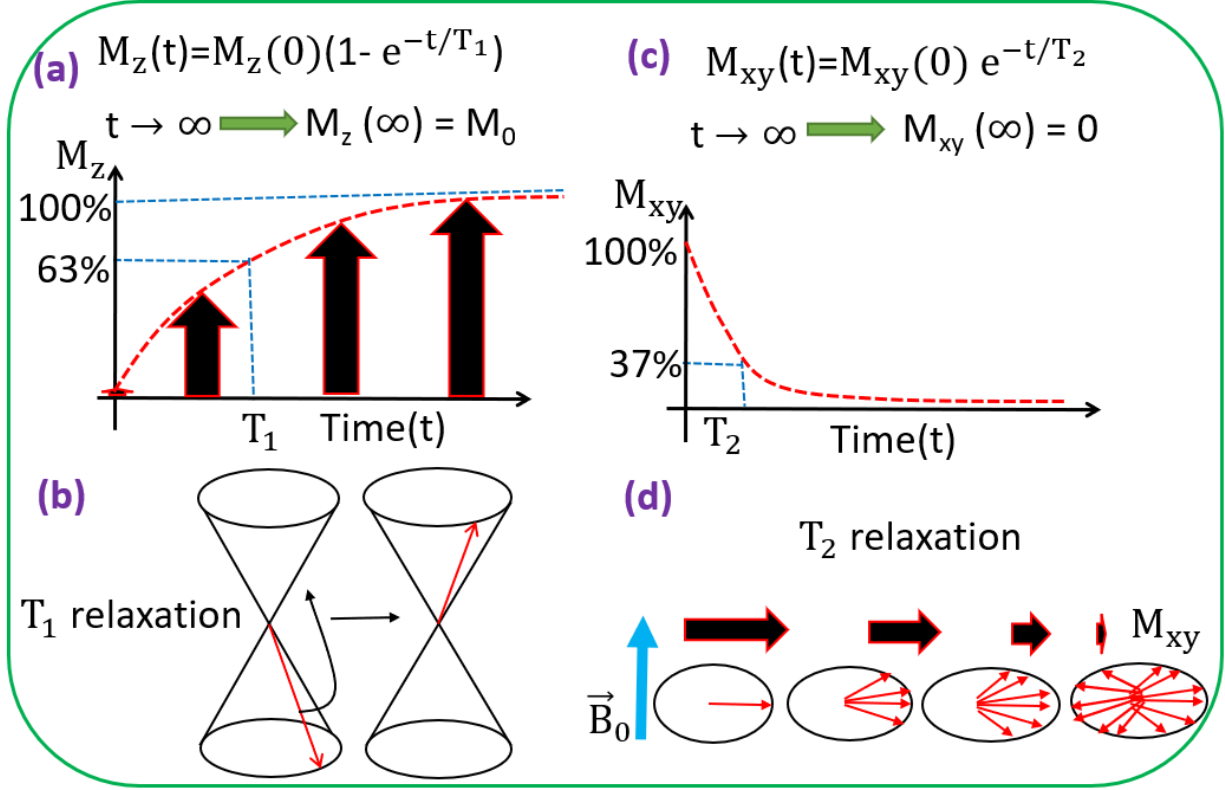


FIG. 3. (a)-(b) When an RF pulse is applied, some spins flip to the higher energy state, decreasing M_z . If the RF pulse is turned off, M_z increases gradually and reaches the initial magnetization M_0 at infinity. When the magnetization reaches to $\sim 63\%$ of M_z it records T_1 . (c)-(d) Once the RF pulse is switched off, the magnetization vector in $x-y$ plane, M_{xy} returns to its initial equilibrium (its maximum value) condition and starts precessing in the $x-y$ plane at different Larmor frequencies, recording T_2 relaxation time at $\sim 37\%$ of M_{xy}

becomes

$$\frac{dM_x(t)}{dt} = \omega_0 M_y(t) - \frac{M_x(t)}{T_2}, \quad (15)$$

$$\frac{dM_y(t)}{dt} = -\omega_0 M_x(t) - \frac{M_y(t)}{T_2}, \quad (16)$$

$$\frac{dM_z(t)}{dt} = \frac{M_0 - M_z(t)}{T_1}. \quad (17)$$

Eq. (17) is known as the Bloch equation for z -magnetization, which characterizes the longitudinal component of the magnetization [34, 54, 56]. The rate of change of z -magnetization with time is inversely proportional to T_1 . It is directly proportional to the difference between the equilibrium value of magnetization, M_0 , and z -magnetization at time t , $M_z(t)$ [see Fig. 3(a)]. The

simplified solution for $M_z(t)$ reads

$$M_z(t) = M_z(0) \exp\left(-\frac{t}{T_1}\right) + M_0 \left(1 - \exp\left(-\frac{t}{T_1}\right)\right). \quad (18)$$

At time $t = 0$ with $M_z(0) = 0$, this expression simplifies to

$$M_z(t) = M_0 \left(1 - \exp\left(-\frac{t}{T_1}\right)\right), \quad (19)$$

which indicates that $M_z(t)$ increases with time, and exponentially approaches the equilibrium value M_0 . Equation (19) shows that the magnetization enhances to $(1 - e^{-1}) \sim 63\%$ of its maximum value in time constant T_1 . When $t \ll T_1$, the equation can be further reduced as $M_z(t) = (t/T_1)M_0$. Moreover, the longitudinal magnetization at $t \rightarrow \infty$ reaches to its equilibrium value $M_z(\infty) = M_0$.

The magnetization in the transverse plane is a complex value as $M_{xy}(t) = M_y(t) + iM_x(t)$. The solutions for $M_{xy}(t)$ can be found by solving the differential equations given by the Bloch equation as

$$\begin{aligned} M_{xy}(t) &= M_{xy}(0) \exp(-i\omega_0 t) \exp\left(-\frac{t}{T_2}\right) \\ &= M_0 \exp(-i\omega_0 t) \exp\left(-\frac{t}{T_2}\right) \\ &= M_0 (\cos(\omega_0 t) - i \sin(\omega_0 t)) \exp\left(-\frac{t}{T_2}\right). \end{aligned} \quad (20)$$

We also mention that M_{xy} at $t = 0$ is defined by $M_{xy}(0) = M_0$. $\text{Re}(M_{xy}(t))$ and $\text{Im}(M_{xy}(t))$ are functions that return the real and imaginary parts of complex number M_{xy} [57, 58]. Therefore

$$M_x(t) = \text{Im}(M_{xy}(t)) = -M_0 \sin(\omega_0 t) \exp\left(-\frac{t}{T_2}\right), \quad (21)$$

$$M_y(t) = \text{Re}(M_{xy}(t)) = M_0 \cos(\omega_0 t) \exp\left(-\frac{t}{T_2}\right). \quad (22)$$

Once M_{xy} exists, magnetization quickly starts vanishing by

$$M_{xy}(t) = M_0 \exp\left(-\frac{t}{T_2}\right). \quad (23)$$

Where M_{xy} vanishes at $t \rightarrow \infty$, as $M_x(\infty) = M_y(\infty) = 0$ [see Fig. 3(b)]. Consequently, the characteristic time T_2 refers to the time it takes for the magnetization to drop to $(1/e)$ of its original value in the presence of the homogeneity field.

A schematic of the dynamics of the elements of the Bloch equation is presented in Fig. 4. This figure provides a geometric visualization of the relaxation process of the NMR magnetization.

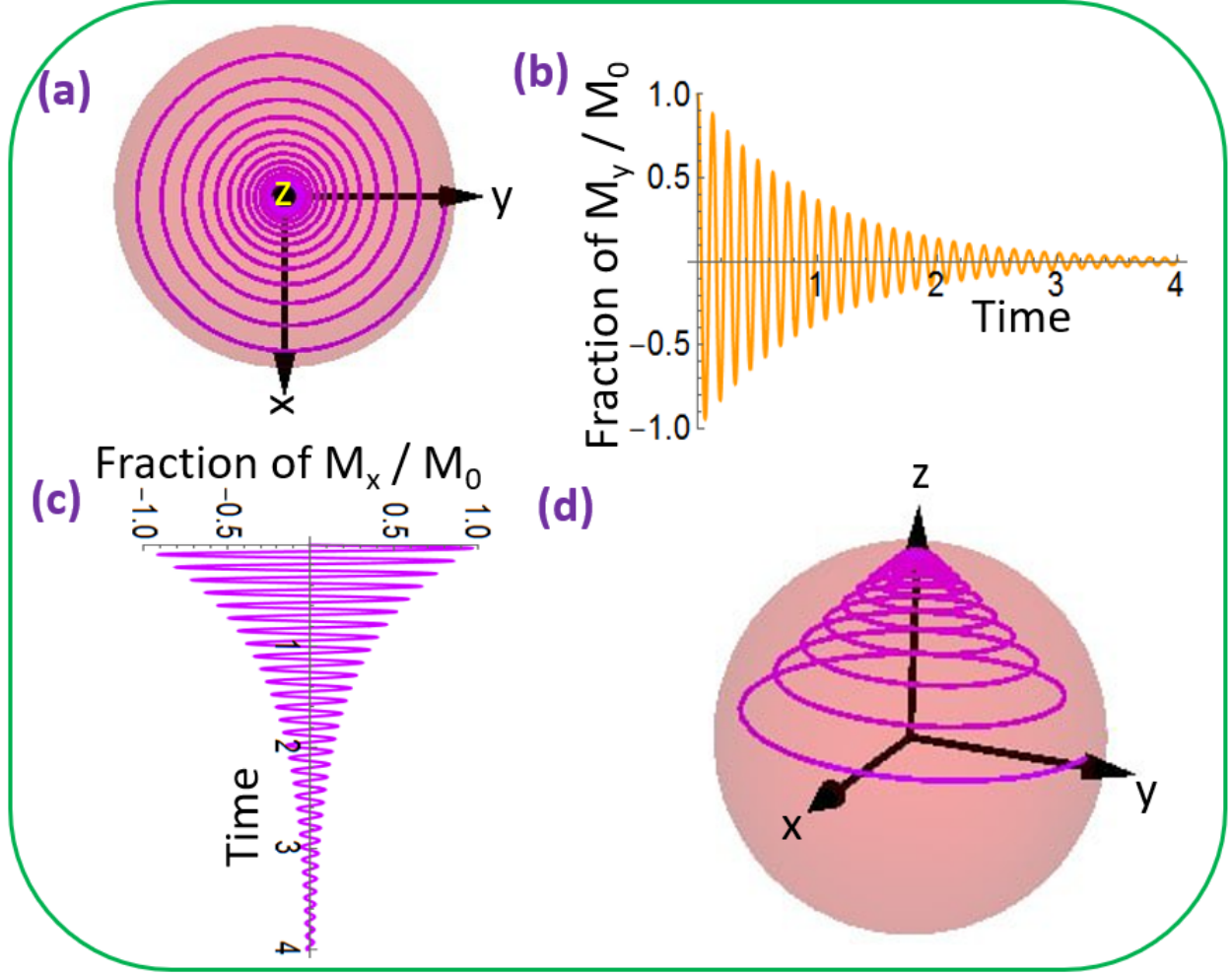


FIG. 4. When an RF pulse is applied, the FID signal is collected. The FT method converts the FID signal to the NMR spectrum: (a) Transverse magnetization in the $x - y$ plane, where the external magnetic field is in the z -axis. (b)-(c) Present the FID signal along the y -axis and x -axis, respectively, where their combination provides (a). (d) The NMR signal is in three dimensions

Accordingly, the system's dynamics in the $x - y$ plane are given in Fig. 4(a). As can readily be seen, the magnetization starting from the y -axis direction processes along the z -axis and decays to the center of the disc in the $x - y$ plane. This process from the point of view of the y - and x -axis can be understood according to Fig. 4(b) and (c), respectively. Including the dynamics in the z -axis, the entire process can be visualized via Fig. 4(d). The comparative dynamics of the y - and x -axis for the initial magnetization in the y -axis direction is depicted in Fig. 4(e).

Equation (23) is known as the FID signal, which is composed of a decaying oscillation sine and cosine functions [see Fig. 4(a)-(d)]. By the FT method, $F(\omega)$, the FID signal converts to the

frequency domain and appears as several peaks on the NMR spectrum. The FT method can be expressed as $F(\omega) = \int_{-\infty}^{+\infty} f(t) \exp(i\omega t) dt$. $F(\omega)$ is a complex function that can be divided into real and imaginary parts as

$$\text{Re}(F(\omega)) = \int_{-\infty}^{+\infty} f(t) \cos(\omega t) dt, \quad \text{Im}(F(\omega)) = \int_{-\infty}^{+\infty} f(t) \sin(\omega t) dt. \quad (24)$$

6. DIFFERENT TYPES OF NMR SPECTROSCOPY

TABLE I. Different types of nucleus with spin quantum number 1/2 and their properties

Nucleus	$\gamma(T^{-1}s^{-1})$	Nat. Abd (%)
1H	2.6752×10^8	100.0
^{13}C	6.7283×10^7	1.11
^{19}F	2.517×10^8	100.0
^{15}N	-2.713×10^7	0.37
^{31}P	1.0841×10^8	100.0

The NMR spectroscopy is a versatile technique that is utilized to study a variety of atomic isotopes with nuclear spin 1/2 such as 1H , ^{13}C , ^{31}P , ^{15}N and ^{19}F . In Table I, we list different types of the nucleus with the spin quantum number 1/2 and present their gyromagnetic ratio γ and natural abundance (Nat. Abd (%)) [17, 59, 60]. In this section, we will consider NMR spectroscopy using the atomic isotopes in Table I.

6.1. Proton Nuclear Magnetic Resonance Spectroscopy

Proton NMR or 1H -NMR is a technique to identify different types of hydrogen atoms that are present in the sample. 1H -NMR is a helpful method for knowing metabolic pathways in living cells. In this technique, the biological sample is dissolved in a solvent as the NMR reference that does not contain protons like deuterium oxide (D_2O) [see Fig. 5(a)] [61, 62].

The 1H -NMR spectrum shows some peaks from 0 to 14 ppm. Analyzing the NMR spectrum gives information about the number, positions, relative intensity, and splitting of signals [44]. This information presents the number of protons in the sample and the number of hydrogens that

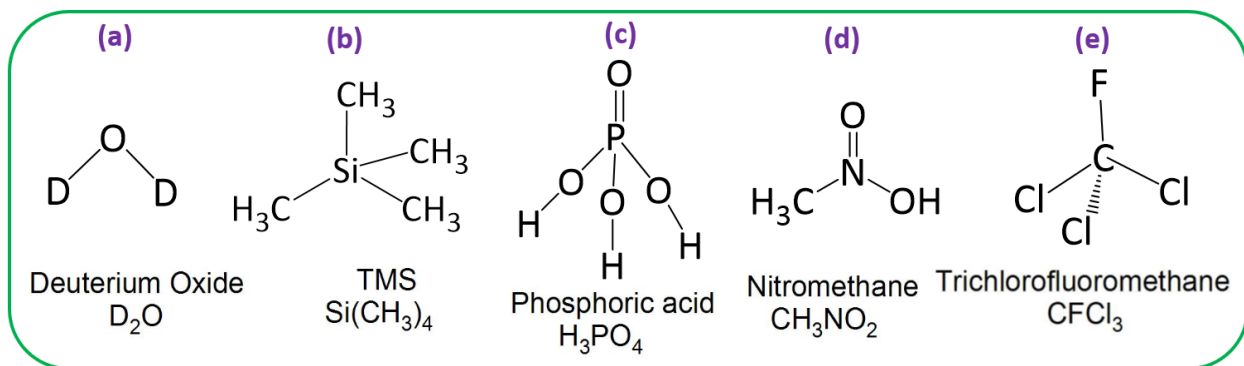


FIG. 5. Scheme of the internal standard reference for different types of NMR: (a) Deuterium oxide (D_2O) for 1H -NMR, (b) TMS ($Si(CH_3)_4$) for ^{13}C -NMR, (c) Phosphoric acid (H_3PO_4) for ^{31}P -NMR, (d) Nitromethane (CH_3NO_2) for ^{15}N -NMR (e) Trichlorofluoromethane ($CFCl_3$) for ^{19}F -NMR

generate the peaks. Moreover, they can show the amount of signal interaction with neighboring hydrogen atoms, which is known as spin splitting [63, 64].

The $n + 1$ rule determines the splitting of proton signals that n is the number of protons in the nearby nuclei. For example, when no hydrogen atom is around the nuclei, the splitting signal from the $n + 1$ rule is a singlet. We present various splitting types in Fig. 6. According to Table I, 1H -NMR is much more sensitive than ^{13}C -NMR because of its highest natural abundance (100%) and largest $\gamma = 2.6752 \times 10^8 T^{-1} s^{-1}$ [40, 65, 66].

6.2. Carbon Nuclear Magnetic Resonance Spectroscopy

NMR is also useful for carbon-based chemical samples like all living systems and organic compounds. Only about 1.11% of all-natural carbons have $1/2$ quantum spin number with $\gamma = 6.7283 \times 10^7 T^{-1} s^{-1}$, which creates ^{13}C nucleus active in NMR imaging and makes it less sensitive than 1H -NMR, as is given in Table I. The ^{13}C -NMR sample should be mixed with a solvent as a reference compound, containing carbon such as TMS ($Si(CH_3)_4$) that makes protons entirely shielded [see Fig. 5(b)] [44, 67–69]. Compared to 1H -NMR spectrum, ^{13}C -NMR peaks are spread from 0 to 200 ppm, which assists in the detection of distinct peaks with a low possibility of signal overlapping in NMR spectroscopy [20, 70, 71].

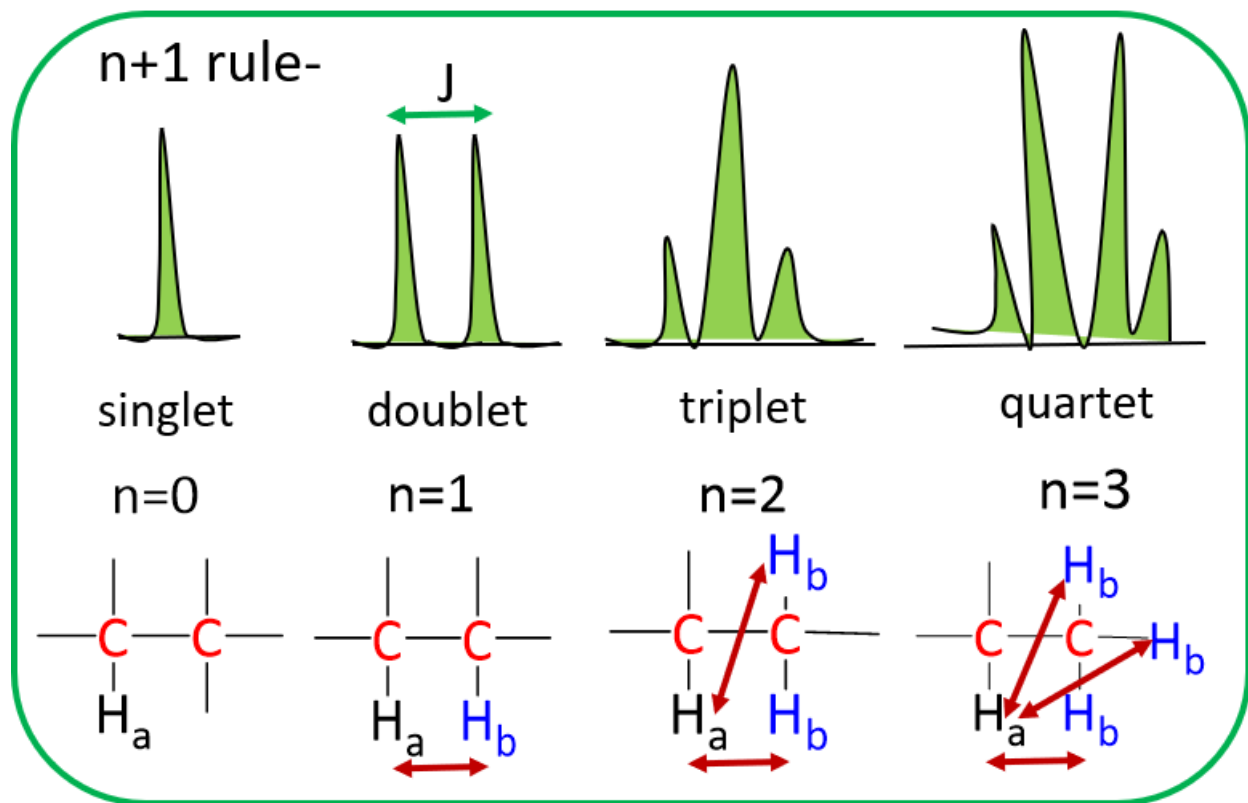


FIG. 6. Splitting patterns in NMR spectroscopy: By $n + 1$ rule, the diversity of the signal is calculated. Singlet signals are not coupled to any protons; doublet signals are coupled to one proton; triplet signals are coupled to two protons; quartet signals are coupled to three protons. The coupling constant, J , is the distance between the peaks in a splitting pattern. Hydrogen nuclei H_a , H_b

6.3. Phosphorus Nuclear Magnetic Resonance Spectroscopy

^{31}P nucleus has 100% natural abundance with $\gamma = 1.0841 \times 10^8 T^{-1} s^{-1}$, which behaves like 1H -NMR. However, ^{31}P chemical shifts cover a broader range compared to 1H -NMR. To achieve ^{31}P -NMR signal, the NMR sample should be mixed with a solvent that contains phosphorus, such as phosphoric acid (H_3PO_4) [see Fig. 5(c)]. From Table I, we see that ^{31}P -NMR has less sensitivity compared to 1H -NMR, and its peak is sharper than the peak of ^{13}C -NMR.

The high natural abundance and large γ make ^{31}P -NMR ideal for studying various systems such as phospholipid liposomes [72], exploring different food characteristics in food science like milk, green tea, and other foods [73, 74]. It is also helpful in detecting cancer tumors in *in vivo* models like breast cancer [75] and lung cancer [76].

6.4. Nitrogen Nuclear Magnetic Resonance Spectroscopy

^{15}N -NMR is a powerful tool for providing useful information about samples that contain nitrogen atoms like RNA/DNA nucleobases [77], molecular structure of organic compounds [78], and soil organic matter [79]. From Table I, we see that ^{15}N -NMR is much less sensitive compared to ^1H -NMR and ^{13}C -NMR, due to the low natural abundance (37%) of ^{15}N nucleus and its small γ value ($\gamma = -2.713 \times 10^7 \text{T}^{-1} \text{s}^{-1}$). Moreover, ^{15}N -NMR chemical shift is significantly wide compared to ^{13}C - and ^1H -NMR, ranging from 0 to 900 ppm. In NMR studies with ^{15}N , Nitromethane (CH_3NO_2) is used as a standard external reference, as demonstrated in Fig. 5(e) [80].

6.5. Fluorine Nuclear Magnetic Resonance Spectroscopy

^{19}F -NMR is a valuable tool for analyzing several amino acids, nucleotides, and sugars that contain fluorine. The ^{19}F nucleus has about 100% natural abundance with large $\gamma = 2.517 \times 10^8 \text{T}^{-1} \text{s}^{-1}$, which has high sensitivity and broader chemical shift dispersion (ranging from -300 to 400 ppm) compared to ^1H -NMR. Therefore, ^{19}F -NMR is a convenient method to investigate important compounds of fluorine-containing pharmaceuticals [81, 82]. In ^{19}F -NMR, Trichlorofluoromethane (CFCl_3) is usually used as a standard reference. The structure of CFCl_3 is shown in Fig. 5(d).

7. PHYSICS OF MAGNETIC RESONANCE IMAGING

MRI is based on the NMR technique utilized for medical imaging. Using MRI as a diagnostic method, we can learn about molecular fields and detect high-resolution images of soft tissues like the brain and cancer tumors [83, 84]. The human body comprises 70% water, containing hydrogen and oxygen atoms. The hydrogen nuclei are the most abundant atoms in the human body. Therefore, we can visualize nuclei of atoms inside the body using MRI and generate powerful signals [60, 85].

The most significant advantage of MRI is its high signal-to-noise ratio because of the strong magnetic field utilized in this technology. MR imaging relies on the main magnetic field, a constant number usually as strong as 1.5-3T. According to the Zeeman effect, hydrogen atoms can align parallel or anti-parallel to \vec{B}_0 . Regarding the Boltzmann distribution, more nuclei stay in the lower energy state than the higher energy state, which results in net magnetization [see Fig. 7] [86].

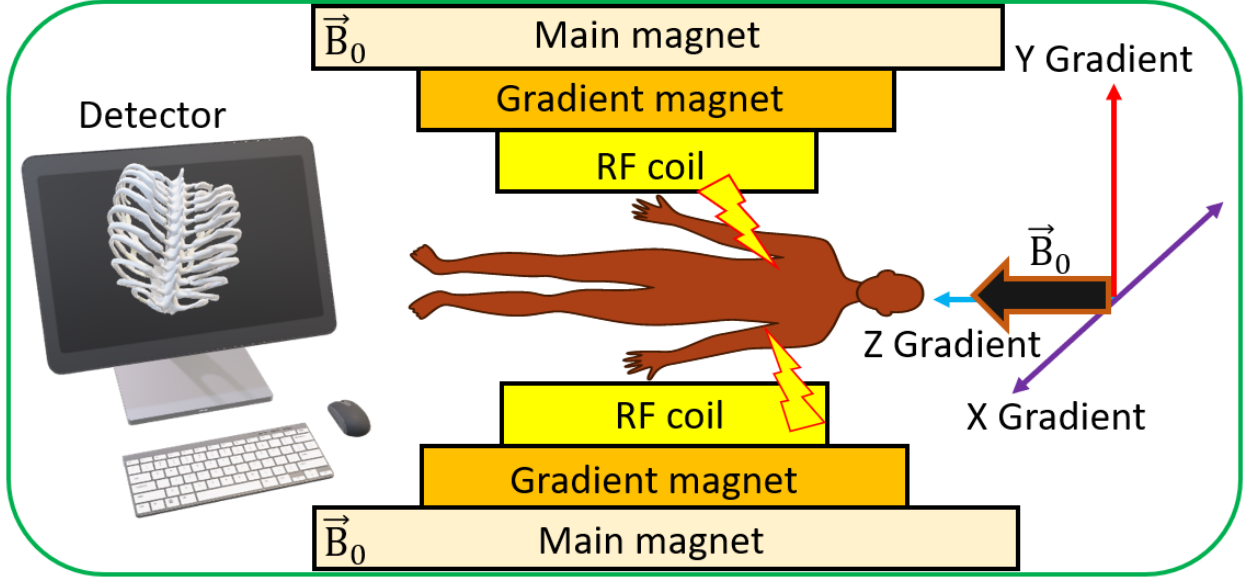


FIG. 7. Scheme of MRI: The locations of main magnet \vec{B}_0 along the z -axis, gradient coils in the x -, y - and z -axis and RF receiver coils are shown in the Scheme. The MRI system is connected to a computer for processing the image of the body

MRI also contains gradient magnets that produce a magnetic field weaker than \vec{B}_0 , known as the second part of the MRI machine. The gradient magnets generate a magnetic field over \vec{B}_0 in the x -, y - and z -axis. Moreover, the gradient magnets modify the strength of \vec{B}_0 and improve precession frequencies on the slice-selection gradient. This process generates spatial encoding for MRI signals [16, 87].

The spatial encoding can be obtained by projecting the signal from all slice spins along the gradient axes. Considering the spatial information obtained from this process, the axial images can be created by the data from the Z-gradient that runs along the long axis. The coronal images can be produced by the data from the Y-gradient, which is along the vertical axis. Finally, the sagittal images can be generated from X-gradient along the horizontal axis [16, 81, 83].

The MRI machine also contains RF coils, which transmit RF pulses into the body and receive signals from the body to produce an image and record it on the screen. The RF coils are designed for specific body regions. These coils are designed to improve the signal-to-noise ratio, which in turn helps to generate better diagnostic images. In this scenario, an RF pulse, \vec{B}_1 , that is orthogonal to \vec{B}_0 and has the precession frequency $\omega(x, y, x) = \gamma B_0(x, y, x)$ should be applied, which turns the net magnetization toward the $x - y$ plane, as was explained in details for the NMR signal.

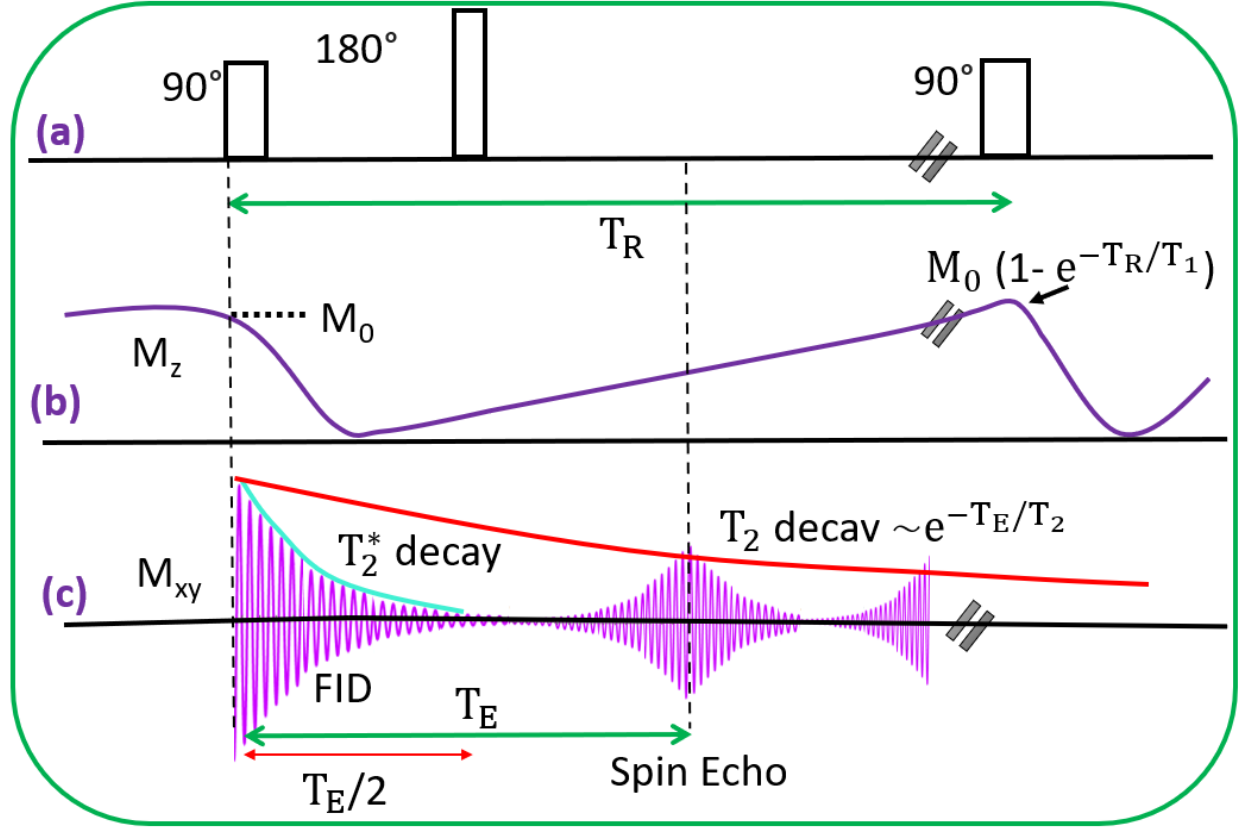


FIG. 8. Scheme of a pulse sequence for producing the spin-echo signal: (a) represents 90-degree RF pulses and 180-degree pulse at $(T_E/2)$ point. (b) The M_z reduces from the start point, M_0 , and grows along the z -axis until the next 90-degree pulses (at T_R point). (c) The M_{xy} flips back into the $x - y$ plane, dephases, and records T_2^* decays or FID signal. The spin echo signal measures and amplitude depend on T_2 at T_E point. The spin echo repeats after T_R point

8. SPIN ECHO PULSE SEQUENCE

The spin-echo sequence is an important pulse sequence used to create an image in MRI. The MRI machine can produce a high-quality image by repeating the pulse sequence several times, known as the spin-echo pulse sequence. The spin-echo pulse sequence refers to a 90-degree RF pulse followed by one or more 180-degree pulses to refocus the spins [88, 89]. This process is shown in Fig. 8. A spin-echo pulse sequence has two important parameters; the time between two 90-degree RF pulses is called repetition time or T_R , and the time between a 90-degree RF pulse and echo-formed signal in MRI, where an echo signal occurs is known as the time to echo or T_E .

These are shown in Fig. 8(a)-(c). The magnitude of M_z at $t = T_R$ is expressed as

$$M_z(T_R) = M_0 \left(1 - \exp \left(-\frac{T_R}{T_1} \right) \right). \quad (25)$$

The FID signal reverses and recovers by applying a 180-degree pulse at $T_E/2$. Then, the magnetization relaxes along the $-z$ -axis and returns to the $+z$ -axis until it reaches its original value M_0 . If a 90-degree RF pulse is applied, at any point during this process, M_z rotates into M_{xy} plane, then a signal can be observed [90, 91].

The dephasing of magnetization causes loss of transverse net magnetization, decaying by T_2 . If magnetization dephases further after the echo, the vectors refocus and form a second echo. By repeating this process, we can form multiple spin echoes. After 90 degree RF pulse, according to Eq. (23), M_{xy} at T_E is

$$M_{xy}(T_E) = M_{xy}(0) \exp(-T_E/T_2). \quad (26)$$

The combination of T_1 and T_2 for a biological tissue can define signal output, $S(r)$, that reads

$$S(r) \simeq \rho \left(1 - \exp \left(-\frac{T_R}{T_1} \right) \right) \exp \left(-\frac{T_E}{T_2} \right), \quad (27)$$

where ρ represents the density of protons per unit tissue. When the larger density of protons (hydrogen atoms) is measured, the brighter signal can be detected on the screen. Therefore, the higher proton density can enhance the image contrast and improve the final MRI signal [92–94].

The other concept that is related to the transverse relaxation is T_2^* decay, which occurs between a 90-degree pulse and $T_E/2$ [see Fig. 8(c)]. In inhomogeneity of field determined by $\Delta B(r)$, which is time-independent, the spin system precesses with Larmor frequency $\omega(r) = \gamma \Delta B(r)$, and $M_{xy}(r, t)$ decays by

$$M_{xy}(r, t) = M_{xy}(r, 0) \exp(-i\gamma \Delta B(r)t). \quad (28)$$

The T_2^* describes decay in the gradient echo (GRE) technique, significantly reducing the scan time. The relation between T_2 and T_2^* is expressed by

$$\frac{1}{T_2^*} = \frac{1}{T_2} + \frac{1}{T_{2i}}, \quad (29)$$

in which T_2 corresponds to signal decays due to spin-spin relaxation, T_{2i} is transverse relaxation due to static magnetic field inhomogeneities that lead to loss of coherence. The T_2^* decays is always less than or equal to T_2 decays.

9. LOW FIELD NMR AND MRI PROPERTIES

The quest for high-resolution MRI has led researchers to perform novel high magnetic field techniques. A high magnetic field MRI is essential to tackle the inherent problem of low magnetic moments in nuclear spins. However, low-field MRI has also been shown to be possible due to progress in MRI techniques. One of the principal advantages of low-field MRI is that it provides a low-cost alternative to high-field instruments for MR imaging.

Moreover, the frequency of operation is much lower for low-field systems. The 0.06T system operates at approximately 2.46 MHz, while a 3T system operates closer to 128 MHz. Moreover, the magnetic field provided at the lower field is significantly homogeneous, making it an excellent clinical research resource [2, 95, 96].

One shortcoming of low-field MRI is that it is sensitive to noise originating from the environment, known as external electromagnetic interference (EMI) signals. There are several developments to prevent and remove EMI during the scan time. Another part of low-field MRI is increasing relaxation time using a contrast agent [97, 98].

We note that some developments in MRI improve the SNR value at low-field MRI. Hyperpolarized (HP) MRI, where dynamic nuclear polarization (DNP) is used to increase the polarization of the spins in an MRI sample, compared with the thermal equilibrium state. HP MRI is better performed at low fields, as the spins relax back to their equilibrium state more slowly.

10. INSIGHTS FROM HEISENBERG UNCERTAINTY PRINCIPLE

In NMR and MRI, the energy operator involved in the spectroscopy is known as energy transition, and the energy operator is called the Hamiltonian (H), which one can attain its eigenvectors and eigenvalues to analyze the system. For presenting the energy values for a nucleus, we should examine the wave function as a sum of all the different states aligned with or against the field, with some probability distributions, depending on the system characteristics [21, 99].

The Heisenberg time-energy uncertainty principle can provide the width of the NMR spectrum or the spectral width (SW) [1, 4, 19, 38]. The uncertainty principle for the nucleus in frequency $\Delta\nu$ and energy dispersion ΔE is given by

$$\Delta t \Delta E \approx \Delta t (h \Delta \nu) \approx h. \quad (30)$$

Also, the nucleus stays on the state at an uncertain lifetime Δt . Then, the peak width line (in

Hz) for the nucleus, which is relaxed back to the lower state in time constant T_2 at frequency ν , is rewritten as

$$\Delta\nu \approx \frac{1}{\Delta t} \approx \frac{1}{T_2}. \quad (31)$$

We can detect the sharper peaks by recording the longer lifetime Δt or increasing relaxation time T_2 , which reduces the resonance linewidth $\Delta\nu$. $\Delta\nu$ refers to the range of the frequencies affected by the lifetime Δt .

11. NMR AND MRI APPLICATION IN MEDICAL SCIENCE

The NMR or MRI sample is collected from either cell culture (*in vitro*) or animal and human model (*in vivo*) experiments, as we present in Fig. 9(a). In *in vitro* setup, the isotope molecules such as ^1H , ^{13}C , ^{31}P , ^{15}N , and ^{19}F are dissolved into special cell culture media and added to cell culture dishes to track their metabolism in the cell. As we mentioned earlier, all isotope molecules have specific standard external references, which are utilized to normalize the output signal from the scanner.

After doping the powder in the cell culture dishes, the extracted cell sample is transferred into the NMR tube and placed in the magnet. Therefore, the final NMR spectrum is processed and displayed on a monitor for further metabolic analysis, as shown in Fig. 9(b). Moreover, for *in vivo* study, the sample is prepared and injected into the body's soft tissue for further analysis.

The NMR technique aims to precisely detect and quantify the metabolic changes in the cells or organs. For MR imaging, depending on the type of study performed, the sample is prepared, and an MRI scanner images the subject. Then, the MRI files are saved in a digital imaging and communications in medicine (DICOM) format and considered for further analysis, as shown in Fig. 9(c).

To be precise about the data analysis steps, we must understand the cells' metabolic pathways and general physiology roles. As represented in Fig. 9(d), glucose metabolism is most organs' primary energy source. Initially, complex glucose molecules are transported into cell membranes via specific transporters. Inside the cell, enzymes break down glucose into simpler forms, generating adenosine triphosphate (ATP), carbon dioxide (CO_2), and water (H_2O) in the mitochondria. The mitochondria play a crucial role in this metabolic pathway. As a last product of the glycolysis pathway, the pyruvate, derived from glycolysis, travels through the TCA or citric acid cycle, contributing to the oxidative phosphorylation process that generates ATP.

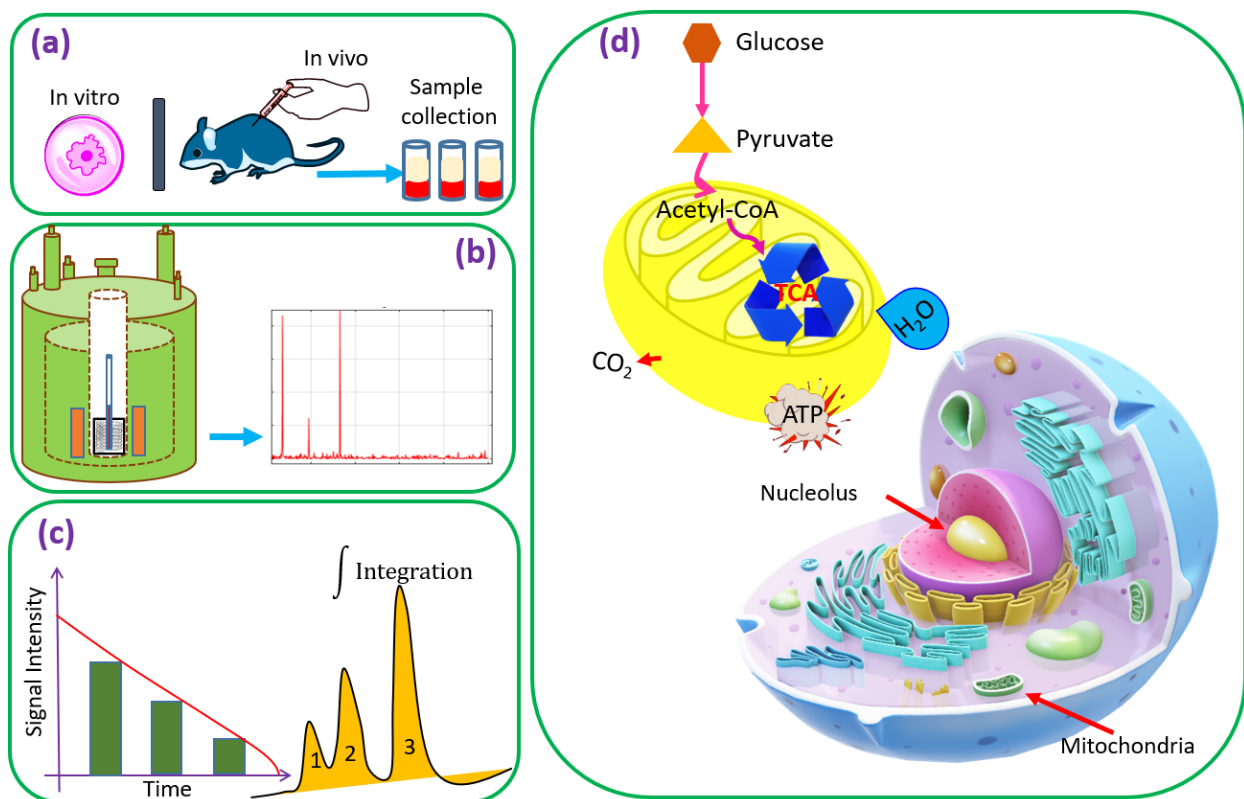


FIG. 9. The basic of NMR data collection: (a) Sample preparation, (b) NMR signal detection, (c) Data analysis, (d) Metabolic pathway

12. CONCLUSION

Nuclear magnetic resonance (NMR) and magnetic resonance imaging (MRI) are versatile tools with broad applications from physics and chemistry to geology and medical studies. In this mini-review, we considered the concepts of NMR and MRI technologies from their fundamental origins to applications in medical science. We started from a quantum mechanical basis and considered the significant importance of NMR and MRI in clinical research. Furthermore, we briefly introduced different types of NMR systems. We also investigated some of the most important applications of MRI techniques to provide valuable methods for visualizing the inside of the body and soft tissues.

-
- [1] J. J. Sakurai and E. D. Commins, *Modern quantum mechanics*, revised edition (1995).
 - [2] D. J. Griffiths and D. F. Schroeter, *Introduction to quantum mechanics* (Cambridge university press, 2018).

- [3] R. P. Feynman, A. R. Hibbs, and D. F. Styer, *Quantum mechanics and path integrals* (Courier Corporation, 2010).
- [4] F. Khashami, *Fundamentals of NMR and MRI: From Quantum Principles to Medical Applications* (Springer Nature Switzerland, 2024).
- [5] Y. Maleki and A. M. Zheltikov, Spin cat-state family for heisenberg-limit metrology, *JOSA B* **37**, 1021 (2020).
- [6] Y. Maleki, M. O. Scully, and A. M. Zheltikov, Quantum metrology with superposition spin coherent states: Insights from fisher information, *Physical Review A* **104**, 053712 (2021).
- [7] Y. Maleki, Quantum phase estimations with spin coherent states superposition, *The European Physical Journal Plus* **136**, 1 (2021).
- [8] R. I. G. Hughes, The bohr atom, models, and realism, *Philosophical Topics* **18**, 71 (1990).
- [9] E. Rutherford and N. F. Mott, Discussion on the structure of atomic nuclei, *Proceedings of the Royal Society of London. Series A, Containing Papers of a Mathematical and Physical Character* **136**, 735 (1932).
- [10] Y. Maleki and M. Suhail Zubairy, Revisiting wave–particle duality in bohr–einstein debate, *AVS Quantum Science* **5** (2023).
- [11] Y. Maleki, J. Liu, and M. S. Zubairy, Quantum eraser from duality-entanglement perspective, *Physical Review A* **104**, 042207 (2021).
- [12] Y. Maleki, Stereographic geometry of coherence and which-path information, *Optics letters* **44**, 5513 (2019).
- [13] F. Khashami, Y. Maleki, and K. Berrada, Entanglement degree of finite-dimensional pair coherent states, *Journal of Russian Laser Research* **34**, 388 (2013).
- [14] Y. Maleki, S. Sheludiakov, V. V. Khmelenko, M. O. Scully, D. M. Lee, and A. M. Zheltikov, Natural and magnetically induced entanglement of hyperfine-structure states in atomic hydrogen, *Physical Review A* **103**, 052804 (2021).
- [15] F. Bloch, W. Hansen, and E. Martin, Packard m. nuclear induction, *Physical Review* **127** (1946).
- [16] K. J. Friston, P. Jezzard, and R. Turner, Analysis of functional mri time-series, *Human brain mapping* **1**, 153 (1994).
- [17] J. D. Roberts and M. C. Caserio, *Basic principles of organic chemistry* (WA Benjamin, Inc., 1977).
- [18] T. Butz, *Fourier transformation for pedestrians* (Springer, 2006).

- [19] I. I. Rabi, J. R. Zacharias, S. Millman, and P. Kusch, A new method of measuring nuclear magnetic moment, *Physical review* **53**, 318 (1938).
- [20] R. Graham and W. Ellington, Anaerobic aspartate metabolism and the formation of alanine in molluscan cardiac muscle: a ^{13}C nmr study, *Journal of Experimental Zoology* **236**, 365 (1985).
- [21] A. Abragam, *The principles of nuclear magnetism*, 32 (Oxford university press, 1983).
- [22] I. Solomon, Relaxation processes in a system of two spins, *Physical Review* **99**, 559 (1955).
- [23] F. Khashami, *Tracking the Biochemistry of Cancer Cells and Dynamics of Physical Systems Using Nuclear Magnetic Resonance*, Ph.D. thesis (2021).
- [24] P. Mansfield, Multi-planar image formation using nmr spin echoes, *Journal of Physics C: Solid State Physics* **10**, L55 (1977).
- [25] J. W. Emsley, J. Feeney, and L. H. Sutcliffe, *High Resolution Nuclear Magnetic Resonance Spectroscopy: Volume 2*, Vol. 2 (Elsevier, 2013).
- [26] D. Davies, Book review: The nuclear overhauser effect in structural and conformational analysis. by d. neuhaus and mp williamson. vch, new york (1989). 522 pp., *Spectrochimica Acta Part A: Molecular Spectroscopy* **47**, 1641 (1991).
- [27] J. B. Ames, Theory and applications of biomolecular nmr spectroscopy, in *Biomedical Applications of Biophysics* (Springer, 2010) pp. 99–118.
- [28] T. Lancaster and S. J. Blundell, *Quantum field theory for the gifted amateur* (OUP Oxford, 2014).
- [29] Y. Maleki, Generation and entanglement of multi-dimensional multi-mode coherent fields in cavity qed, *Quantum Information Processing* **15**, 4537 (2016).
- [30] E. M. Purcell, H. C. Torrey, and R. V. Pound, Resonance absorption by nuclear magnetic moments in a solid, *Physical review* **69**, 37 (1946).
- [31] R. Damadian, Field focusing nmr (fonar) and the formation of chemical images in man, *Philosophical Transactions of the Royal Society of London. B, Biological Sciences* **289**, 489 (1980).
- [32] A. Y. Kitaev, A. Shen, and M. N. Vyalyi, *Classical and quantum computation*, 47 (American Mathematical Soc., 2002).
- [33] L. De Broglie, The reinterpretation of wave mechanics, *Foundations of Physics* **1**, 5 (1970).
- [34] J. D. Jackson, *Classical electrodynamics* (1999).
- [35] P. C. Lauterbur, Image formation by induced local interactions: examples employing nuclear magnetic resonance, *nature* **242**, 190 (1973).

- [36] S. C. Bushong and G. Clarke, *Magnetic Resonance Imaging-E-Book: Physical and Biological Principles* (Elsevier Health Sciences, 2013).
- [37] R. Hashemi, W. Bradley, and C. Lisanti, Basic principles of mri, in *MRI: the basics* (Lippincott Williams & Wilkins, Philadelphia, 2010) pp. 16–31.
- [38] W. Heisenberg, *Encounters with Einstein: And other essays on people, places, and particles*, Vol. 4 (Princeton University Press, 1989).
- [39] Y. Maleki, F. Khashami, and Y. Mousavi, Entanglement of three-spin states in the context of su (2) coherent states, *International Journal of Theoretical Physics* **54**, 210 (2015).
- [40] M. H. Levitt, R. Freeman, and T. Frenkiel, Broadband heteronuclear decoupling, *Journal of Magnetic Resonance* (1969) **47**, 328 (1982).
- [41] F. Schwabl, *Statistical mechanics* (Springer Science & Business Media, 2013).
- [42] Y. Maleki and B. Ahansaz, Quantum correlations in qutrit-like superposition of spin coherent states, *Laser Physics Letters* **16**, 075205 (2019).
- [43] A. Stoneham, Shapes of inhomogeneously broadened resonance lines in solids, *Reviews of Modern Physics* **41**, 82 (1969).
- [44] M. H. Levitt, *Spin dynamics: basics of nuclear magnetic resonance* (John Wiley & Sons, 2013).
- [45] V. Bakmutov, How and why nuclei relax, *Practical NMR relaxation for chemists* , 4 (2004).
- [46] V. Y. Shifrin, P. G. Park, V. N. Khorev, C. H. Choi, and C. S. Kim, A new low-field determination of the proton gyromagnetic ratio in water, *IEEE Transactions on Instrumentation and Measurement* **47**, 638 (1998).
- [47] D. Posener, The shape of spectral lines: Tables of the voigt profile, *Australian Journal of Physics* **12**, 184 (1959).
- [48] Y. Maleki and A. M. Zheltikov, Perfect swap and transfer of arbitrary quantum states, *Optics Communications* **496**, 126870 (2021).
- [49] Y. Maleki and A. M. Zheltikov, Recovery of maximally entangled quantum states by weak-measurement reversal, *Laser Physics Letters* **15**, 056201 (2018).
- [50] Y. Maleki, Entanglement and decoherence in two-dimensional coherent state superpositions, *International Journal of Theoretical Physics* **56**, 757 (2017).
- [51] S. Vathyam, S. Lee, and W. S. Warren, Homogeneous nmr spectra in inhomogeneous fields, *Science* **272**, 92 (1996).

- [52] G. C. Levy and I. R. Peat, The experimental approach to accurate carbon-13 spin-lattice relaxation measurements, *Journal of Magnetic Resonance* (1969) **18**, 500 (1975).
- [53] R. E. Sepponen, J. A. Pohjonen, J. T. Sipponen, and J. I. Tantt, A method for t1 rho imaging., *Journal of computer assisted tomography* **9**, 1007 (1985).
- [54] K. Shrivastava, Theory of spin–lattice relaxation, *physica status solidi (b)* **117**, 437 (1983).
- [55] R. Orbach, Spin-lattice relaxation in rare-earth salts, *Proceedings of the Royal Society of London. Series A. Mathematical and Physical Sciences* **264**, 458 (1961).
- [56] P. A. Tipler and R. Llewellyn, *Modern physics* (Macmillan, 2003).
- [57] D. H. McIntyre, Spin and quantum measurement, *Quantum* **1**, 4 (2002).
- [58] P.-K. Wang and C. P. Slichter, A pictorial operator formalism for nmr coherence phenomena, *Bull. Magnetic Resonance* **8**, 3 (1986).
- [59] K. Golman and J. S. Petersson, Metabolic imaging and other applications of hyperpolarized ^{13}C , *Academic radiology* **13**, 932 (2006).
- [60] A. Filler, The history, development and impact of computed imaging in neurological diagnosis and neurosurgery: Ct, mri, and dti, *Nature precedings* , 1 (2009).
- [61] A. Legchenko and P. Valla, A review of the basic principles for proton magnetic resonance sounding measurements, *Journal of Applied Geophysics* **50**, 3 (2002).
- [62] J. Y. Jung, H.-S. Lee, D.-G. Kang, N. S. Kim, M. H. Cha, O.-S. Bang, D. H. Ryu, and G.-S. Hwang, 1h-nmr-based metabolomics study of cerebral infarction, *Stroke* **42**, 1282 (2011).
- [63] D. Rugar, R. Budakian, H. Mamin, and B. Chui, Single spin detection by magnetic resonance force microscopy, *Nature* **430**, 329 (2004).
- [64] C. Westbrook and J. Talbot, *MRI in Practice* (John Wiley & Sons, 2018).
- [65] C. P. Slichter, *Principles of magnetic resonance*, Vol. 1 (Springer Science & Business Media, 2013).
- [66] K. Krynicky, Proton spin-lattice relaxation in pure water between 0 c and 100 c, *Physica* **32**, 167 (1966).
- [67] R. W. Darbeau, Nuclear magnetic resonance (nmr) spectroscopy: a review and a look at its use as a probative tool in deamination chemistry, *Applied Spectroscopy Reviews* **41**, 401 (2006).
- [68] D. M. Grant and E. G. Paul, Carbon-13 magnetic resonance. ii. chemical shift data for the alkanes, *Journal of the American Chemical Society* **86**, 2984 (1964).
- [69] J. Schaefer and E. Stejskal, Carbon-13 nuclear magnetic resonance of polymers spinning at the magic angle, *Journal of the American Chemical Society* **98**, 1031 (1976).

- [70] N. D. Soni, A. Ramesh, D. Roy, and A. B. Patel, Brain energy metabolism in intracerebroventricularly administered streptozotocin mouse model of alzheimer's disease: A 1h-[13c]-nmr study, *Journal of Cerebral Blood Flow & Metabolism* **41**, 2344 (2021).
- [71] U. Sonnewald, N. Westergaard, S. Petersen, G. Unsgård, and A. Schousboe, Metabolism of [u-13c] glutamate in astrocytes studied by 13c nmr spectroscopy: incorporation of more label into lactate than into glutamine demonstrates the importance of the tricarboxylic acid cycle, *Journal of neurochemistry* **61**, 1179 (1993).
- [72] M. A. Dubinnyi, D. M. Lesovoy, P. V. Dubovskii, V. V. Chupin, and A. S. Arseniev, Modeling of 31p-nmr spectra of magnetically oriented phospholipid liposomes: A new analytical solution, *Solid state nuclear magnetic resonance* **29**, 305 (2006).
- [73] G. I. Gall, I. Colquhoun, *et al.*, Nmr spectroscopy in food authentication., *Food authenticity and traceability* , 131 (2003).
- [74] J.-P. Renou, Nmr studies in meat, in *Annual reports on NMR spectroscopy*, Vol. 31 (Elsevier, 1995) pp. 313–344.
- [75] P. F. Daly, R. C. Lyon, P. J. Faustino, and J. S. Cohen, Phospholipid metabolism in cancer cells monitored by 31p nmr spectroscopy., *Journal of Biological Chemistry* **262**, 14875 (1987).
- [76] T. Ng, W. Evanochko, R. Hiramoto, V. Ghanta, M. Lilly, A. Lawson, T. Corbett, J. Durant, and J. Glickson, 31p nmr spectroscopy of in vivo tumors, *Journal of Magnetic Resonance* (1969) **49**, 271 (1982).
- [77] R. P. Barnwal, F. Yang, and G. Varani, Applications of nmr to structure determination of rnas large and small, *Archives of biochemistry and biophysics* **628**, 42 (2017).
- [78] W. von Philipsborn and R. Müller, 15n-nmr spectroscopy—new methods and applications [new analytical methods (28)], *Angewandte Chemie International Edition in English* **25**, 383 (1986).
- [79] N. Mathers, X. Mao, P. Saffigna, Z. Xu, S. Berners-Price, and M. Perera, Recent advances in the application of 13c and 15n nmr spectroscopy to soil organic matter studies, *Soil Research* **38**, 769 (2000).
- [80] T. Khin and G. Webb, Some indo calculations of nitrogen-nitrogen spin-spin coupling constants, *Journal of Magnetic Resonance* (1969) **33**, 159 (1979).
- [81] A. O. Okaru, T. S. Brunner, S. M. Ackermann, T. Kuballa, S. G. Walch, M. Kohl-Himmelseher, and D. W. Lachenmeier, Application of 19f nmr spectroscopy for content determination of fluorinated pharmaceuticals, *Journal of analytical methods in chemistry* **2017** (2017).

- [82] J.-X. Yu, R. R. Hallac, S. Chiguru, and R. P. Mason, New frontiers and developing applications in 19f nmr, *Progress in nuclear magnetic resonance spectroscopy* **70**, 25 (2013).
- [83] D. B. Plewes and W. Kucharczyk, Physics of mri: a primer, *Journal of magnetic resonance imaging* **35**, 1038 (2012).
- [84] M. A. Bernstein, K. F. King, and X. J. Zhou, *Handbook of MRI pulse sequences* (Elsevier, 2004).
- [85] M. L. Hirsch, N. Kalechofsky, A. Belzer, M. Rosay, and J. G. Kempf, Brute-force hyperpolarization for nmr and mri, *Journal of the American Chemical Society* **137**, 8428 (2015).
- [86] D. Canet, G. C. Levy, and I. R. Peat, Time saving in 13c spin-lattice relaxation measurements by inversion-recovery, *Journal of Magnetic Resonance* (1969) **18**, 199 (1975).
- [87] K. P. Pruessmann, M. Weiger, M. B. Scheidegger, and P. Boesiger, Sense: sensitivity encoding for fast mri, *Magnetic Resonance in Medicine: An Official Journal of the International Society for Magnetic Resonance in Medicine* **42**, 952 (1999).
- [88] W. Yao, N. Qu, Z. Lu, and S. Yang, The application of t1 and t2 relaxation time and magnetization transfer ratios to the early diagnosis of patellar cartilage osteoarthritis, *Skeletal radiology* **38**, 1055 (2009).
- [89] T. J. Mosher and B. J. Dardzinski, Cartilage mri t2 relaxation time mapping: overview and applications, in *Seminars in musculoskeletal radiology*, Vol. 8 (Copyright© 2004 by Thieme Medical Publishers, Inc., 333 Seventh Avenue, New . . . , 2004) pp. 355–368.
- [90] P. J. Basser, J. Mattiello, and D. LeBihan, Estimation of the effective self-diffusion tensor from the nmr spin echo, *Journal of Magnetic Resonance, Series B* **103**, 247 (1994).
- [91] B. Antalek, Using pulsed gradient spin echo nmr for chemical mixture analysis: how to obtain optimum results, *Concepts in Magnetic Resonance: An Educational Journal* **14**, 225 (2002).
- [92] M. Styner, C. Brechbuhler, G. Szckely, and G. Gerig, Parametric estimate of intensity inhomogeneities applied to mri, *IEEE transactions on medical imaging* **19**, 153 (2000).
- [93] H. Chang and J. M. Fitzpatrick, A technique for accurate magnetic resonance imaging in the presence of field inhomogeneities, *IEEE transactions on medical imaging* **11**, 319 (1992).
- [94] U. Vovk, F. Pernus, and B. Likar, A review of methods for correction of intensity inhomogeneity in mri, *IEEE transactions on medical imaging* **26**, 405 (2007).
- [95] M. S. Albert, D. F. Kacher, D. Balamore, A. K. Venkatesh, and F. A. Jolesz, T1 of 129xe in blood and the role of oxygenation (1999).

- [96] J. C. Maxwell, On a dynamical theory of the electromagnetic field, Proceedings of the Royal Society of London , 531 (1864).
- [97] R. P. Feynman, R. B. Leighton, and M. Sands, *The Feynman lectures on physics, Vol. I: The new millennium edition: mainly mechanics, radiation, and heat*, Vol. 1 (Basic books, 2011).
- [98] J. Bardeen, L. N. Cooper, and J. R. Schrieffer, Theory of superconductivity, Physical review **108**, 1175 (1957).
- [99] E. Schrödinger, An undulatory theory of the mechanics of atoms and molecules, Physical review **28**, 1049 (1926)